An electronic structure study of acetone by electron momentum spectroscopy: a comparison with SCF, MRSD-CI and density functional theory

Y. Zheng [a], J.J. Neville [a], C.E. Brion [a], Y. Wang [b], E.R. Davidson [b]

[a] Department of Chemistry, The University of British Columbia, Vancouver, B.C., Canada V6T 1Z1
[b] Department of Chemistry, Indiana University, Bloomington, IN 47405, USA

Abstract

The binding energy spectra and momentum distributions of all valence orbitals of acetone have been studied by electron momentum spectroscopy (EMS) and SCF, MRSD-CI, and density functional theory (DFT) calculations. The experiment was performed using a multichannel EMS spectrometer at a total energy of 1200 eV. Binding energy spectra measured in the energy range of 6–60 eV are compared with the results of OVGF and 2ph-TDA many-body Green's function calculations. In the inner valence region strong splitting of the $5a_1$ and $4a_1$ orbitals due to final state electron correlation is observed. The distribution of energies and pole strengths predicted by the Green's function calculations deviates considerably from the measured ionization energies and strengths in the innervalence region. The measured momentum distributions are compared with calculations at the level of the target Hartree–Fock approximation (THFA) using the SCF method and the target Kohn–Sham approximation (TKSA) using DFT and the local-density approximation. Basis sets used for the SCF calculations ranged from the simplest (STO-3G) to large (204-GTO) and for the DFT calculations very large atomic natural orbital (ANO) basis sets were used. The effects of electron correlation and relaxation are also investigated in MRSD-CI calculations of the full ion–neutral overlap amplitude using large and saturated basis sets. In general, the THFA model with an intermediate basis set and very diffuse functions ($6-311 + +G^{**}$) and with a near Hartree–Fock limit SCF wavefunction (204-GTO), and the TKSA-DFT model with an ANO basis set all provide reasonable predictions of momentum distributions for most orbitals. However, none of these calculations gives a completely satisfactory description of the momentum distribution of the HOMO ($5b_2$) orbital.

1. Introduction

A detailed knowledge of molecular electronic structure and electron behaviour, particularly in the outer valence orbitals, is a key factor in understanding chemical properties including reactivity. A prime consideration in molecular electronic structure is the electron density distribution which is given by integration of the square of the molecular electronic wavefunction, $|\Psi(r)|^2$, over the electron positions and spins. There-fore it is important to have an accurate knowledge of the electron density in all r regions, including the large r region (i.e. effectively the small momentum (p) region), where chemical reactivity is initiated as two species approach each other. It has been demonstrated that a direct imaging of the electron density in momentum space for binding energy selected electrons (i.e. effectively for individual molecular orbitals) can be achieved by electron momentum spectroscopy (EMS) [1–6].

Electron momentum spectroscopy is based on an electron–molecule impact ionization, or (e, 2e), reaction in the knockout kinematic region. At high enough energies and momentum transfer electron–electron collision is dominant and the plane wave impulse approximation (PWIA) applies. Under these conditions and in the symmetric non-coplanar geometry [1–6], i.e. two outgoing electrons with the same energies scattered at the same polar angles, the measured angular correlation between the two outgoing electrons is directly proportional to the square overlap of the initial molecular wavefunction and the final ion wavefunction. This overlap is known as the Dyson orbital of the ionized electron. If the target is well described by the single particle approximation (i.e. the target Hartree–Fock approximation (THFA)) the Dyson orbital is approximately proportional to a canonical Hartree–Fock orbital and the (e, 2e) cross section provides a direct measurement of the orbital electron density in momentum space, $| \phi(p) |^2$. This is usual referred to as the momentum distribution of a bound electron in a molecular target for a given binding energy, i.e. a given molecular orbital. Therefore to a very good approximation EMS provides individual "orbital images" of the electron density in momentum space. In practice the results are spherically averaged due to the random orientation of the gaseous target molecules. Since the impulse approximation works very well in the small momentum region ($p \leqslant 1.5$ au) EMS sensitively probes molecular wavefunctions particularly in the large r region.

In the last two decades many experiments on atoms and small molecules [1–5] have demonstrated that electron momentum spectroscopy is a powerful and informative experimental tool for studying the electronic structure of atoms and molecules, and that it can provide extremely detailed information on electron motion and also the role of electron correlation in atoms and molecules. This information has lead to improved theoretical models for the electronic wavefunctions of atoms and molecules [1,3,5] at both SCF and CI levels of treatment. The results have also provided improved understanding of the relation between electron density distribution and chemical reactivity [7,8]. Using EMS, various wavefunction models including the Hartree–Fock and very large many-body treatments such as CI have been evaluated for the simple "benchmark" systems, H_2O [9,5], NH_3 [7,8] and HF [10]. Some more

complex polyatomic systems, such as SF_6 [11] and $(CH_3)_2O$ [12,13], have been also investigated by comparing the EMS results with SCF calculations.

Electronic structure information on the reactive parts of electron distributions of biological and biochemical molecules is of potential importance in many applications, such as for example biochemistry, medicine and drug design. However, at present only very approximate and largely untested wavefunctions are available for larger molecules. Such limited accuracy wavefunctions would for example be of little use for computer aided molecular design studies which at present use total charge densities obtained from molecular potentials. Based upon our experience in the evaluation and design of accurate wavefunctions for small molecules, we now plan to extend EMS studies to larger polyatomic molecules and eventually to prototypical biological and biochemical molecules [14]. The experimental difficulties related to those large molecular systems are their low volatilities, low signal strengths and closely spaced orbital energies. In order to perform sufficiently accurate EMS experiments on larger molecules it is necessary to use a multichannel EMS spectrometer to increase the rate of data accumulation over that of conventional single channel instruments [15]. The energy resolution of the spectrometer should also be improved to resolve the more closely spaced valence orbitals. As far as theory is concerned, large extended and diffuse basis sets are needed for accurate high level SCF and CI calculations of momentum distributions and thus the SCF and CI methods are necessarily limited to small molecules due to the computational complexity. Therefore alternative theoretical methods are needed to perform relatively high level calculations for more complex systems such as biological and biochemical molecules.

In order to extend EMS studies to larger molecules an energy dispersive multichannel EMS spectrometer with microchannel plates (MCP) and resistive anodes (RA) has been constructed in this laboratory at the University of British Columbia. The spectrometer is similar in design to equipment developed earlier at the Flinders University of South Australia [11,16,17]. The instrument typically has an energy resolution of 1.4 eV FWHM and a momentum resolution of ~0.1 au FWHM. The data accumulation rate using this multichannel spectrometer is significantly increased over that using our earlier reported single channel instrument

[15]. A further feature of the multichannel system is that the momentum distributions of two closely spaced orbitals (with separation energy difference as little as 0.8 eV) can be obtained by curve fitting multichannel binding energy spectra, obtained at various azimuthal angles, using known energy positions and widths from high resolution photoelectron spectroscopy. Therefore, using the multichannel spectrometer and the above-mentioned method of data analysis EMS experiments on larger molecules should be possible.

On the theoretical side, Kohn–Sham (KS) density functional theory (DFT) using the local-density approximation and target Kohn–Sham approximation (TKSA) with large atomic natural orbital basis sets has recently been investigated by Duffy, Chong, Casida and Salahub for calculating the orbital momentum distributions of molecules [18]. DFT theory has been successfully applied to large systems in solid state physics, organic and biological chemistry [19,20]. Kohn–Sham DFT theory provides an alternative to conventional ab initio methods such as SCF and CI and the quality of DFT results is typically comparable to or better than Hartree–Fock for calculations of many properties for some small and large molecules [21,22]. It has been shown that, although Kohn–Sham orbitals are not Dyson orbitals, they approximate Dyson orbitals in a well-defined variational sense [18,23]. Thus it is of interest to compare theoretical electron momentum profiles calculated using DFT in the TKSA approximation with SCF and CI calculations and also with the experimental momentum profiles. The main advantage of using the TKSA is that the computational savings afforded by DFT allow for calculations of momentum distributions of much larger systems. Therefore, it is of interest to see if the TKSA will give sufficiently accurate calculations of momentum distributions for a larger molecule such as acetone where high level SCF and many-body CI treatments are available [15]. If this is the case then the TKSA-DFT treatments can be extended with some confidence to even larger systems such as prototypical biochemicals and other species of biological interest.

With the above perspective in mind the acetone molecule has been chosen for our first EMS studies using the multichannel EMS spectrometer and the TKSA-DFT theoretical model. This molecule has 10 atoms and 32 electrons, thus it is a relatively large molecular system from a theoretical standpoint. Near SCF limit calculations (204-GTO) have been performed for all the valence orbitals of acetone and high level many-body calculations (204-G(CI)) for the HOMO ($5b_2$) and $2b_1$ orbitals are also available [15]. Thus, the TKSA-DFT model can be used to calculate the momentum distributions of various orbitals and the results can then be compared with the high level SCF and CI results [15]. While the momentum distribution of the HOMO orbital of acetone has been previously measured using a single channel EMS spectrometer [15], the statistics of the single channel data were poor due to the very low cross section, even though a very long data collection time was used. In particular the cross section is extremely low around the second peak of the momentum distribution and the large scatter of the single channel data precludes a quantitative evaluation of theory in this region [15]. More accurate experimental data for this orbital are therefore needed to provide an accurate evaluation of the various calculations.

In the present work we now report the first complete EMS data of the valence orbitals of acetone, including the binding energy spectra from 6 to 60 eV and the momentum distributions of all the valence orbitals, obtained using the multichannel EMS spectrometer. The details of this new instrument and its performance are also presented. The binding energy spectra are compared with OVGF and 2ph-TDA many-body Green's function calculations using a (9s5p/4s)/[4s2p/2s] basis set (see Ref. [24] for details). The measured momentum distributions are compared with three calculations, namely the SCF calculations using the intermediate (6-311++G**) and near-Hartree–Fock limit (204-GTO) basis sets and the TKSA-DFT calculations using the local-density approximation with large atomic natural orbital (ANO) basis sets. In addition a particularly detailed study has been made of the highest occupied molecular orbital (HOMO) and two independent experimental methods have been used to obtain this momentum distribution. The measured momentum distribution of the HOMO orbital is compared with various calculations using SCF wavefunctions ranging from the minimal STO-3G basis set to the near Hartree–Fock limit. In addition TKSA-DFT and many-body configuration interaction (CI) treatments with large and saturated basis sets are also compared with the HOMO measurements.

2. Experimental methods

The energy-dispersive multichannel EMS spectrometer used in the present experiment is similar in overall design and concept to equipment used earlier at the Flinders University of South Australia [11,16,17]. Fig. 1 shows a schematic diagram of the multichannel EMS spectrometer. The whole instrument is in a μ-metal shielded vacuum system, which is evacuated by two Seiko-Seiki TMP 450 MAGLEV turbomolecular pumps for the main chamber and one TMP 300 MAGLEV turbomolecular pump for the differentially pumped electron gun system. A base pressure of 10^{-7} Torr is achieved.

A thoriated tungsten wire filament provides electrons that are accelerated and focused into the interaction region by a vertically mounted, commercially available, electron gun (Cliftronics CE5AH). Two Einzel lenses are used to focus the electron beam due to the long length between the gun and interaction region. Three sets of quad parallel plate deflectors and four
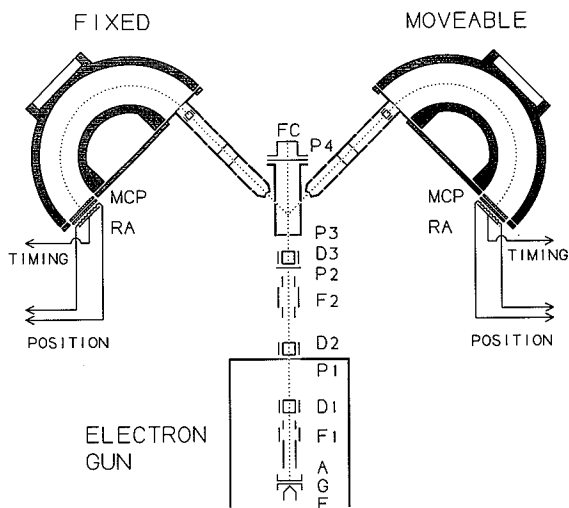

Fig. 1. Schematic diagram of the non-coplanar symmetric multichannel EMS spectrometer showing the geometrical arrangement of the electron gun, interaction region, analysers and position sensitive detectors. The polar angles θ of the fixed and movable analysers are kept fixed at 45° and the out-of-plane azimuthal angle ϕ of the movable analyser is varied. The vertical incident electron beam is along the z-axis. A, G and F are the anode, grid, and filament respectively; F1 and F2 are Einzel lenses; D1, D2 and D3 are quad parallel deflectors; P1, P2, P3 and P4 are spray plate apertures; FC is the Faraday cup; MCPs are microchannel plates; RAs are resistive anodes.

spray plate apertures and a Faraday cup are used to align the electron beam into the interaction region and to monitor the beam current in various stages. A well-focused electron beam (~ 1 mm in diameter) with a high beam current (typically 30–40 μA) is obtained in the interaction region.

Two hemispherical analysers [25] of mean radius 70 mm with multichannel detectors are used for selecting energetically and detecting the scattered and ejected electrons in the experiment. The polar angles θ of the two hemispherical analysers can be varied over the range of $\pm 5°$, so that a sufficient momentum range of bound core electrons can be studied in future experiments on site-specific electron densities. The analysers are set to $\theta = 45°$ for present applications. The relative azimuthal angle ϕ between the two analyser systems can be varied over a range of $\pm 50°$ under computer control. A five-element electron optical lens system is used in each analyser. The lens system consists of two zoom lenses [26]. The first zoom lens controls the acceptance angle of the detector, and thus the angular resolution of the spectrometer. The retardation and energy resolution of the instrument are affected by the second zoom lens. The electrons are linearly dispersed by each hemispherical analyser according to their input energies along the radius direction at the exit focal plane. A one-dimensional energy dispersive position sensitive detector is then used to measure the electrons at the exit plane. The position sensitive detectors have been constructed using two 25 mm diameter microchannel plates (Electro Optical Sensors type, VUW8946ZS) in the double chevron configuration [27] and a Gear type resistive anode [28].

The electronics used for the energy determination and the fast timing logic and also for the computer interfacing are shown schematically in Fig. 2. The two position signal output pulses from each resistive anode are amplified by Ortec preamplifiers (142IH) and amplifiers (855). Two Ortec 464 charge division units (position sensitive detector analysers (PSDA)) are then used to decode the position information of the detected electrons. The timing signals are taken from the back of each resistive anode using a gold plated copper strip plate and following amplification and discrimination are detected in coincidence using a time-to-amplitude converter (TAC). True and accidental (random) coincidences are detected separately using single channel analysers (SCA). The summed posi-
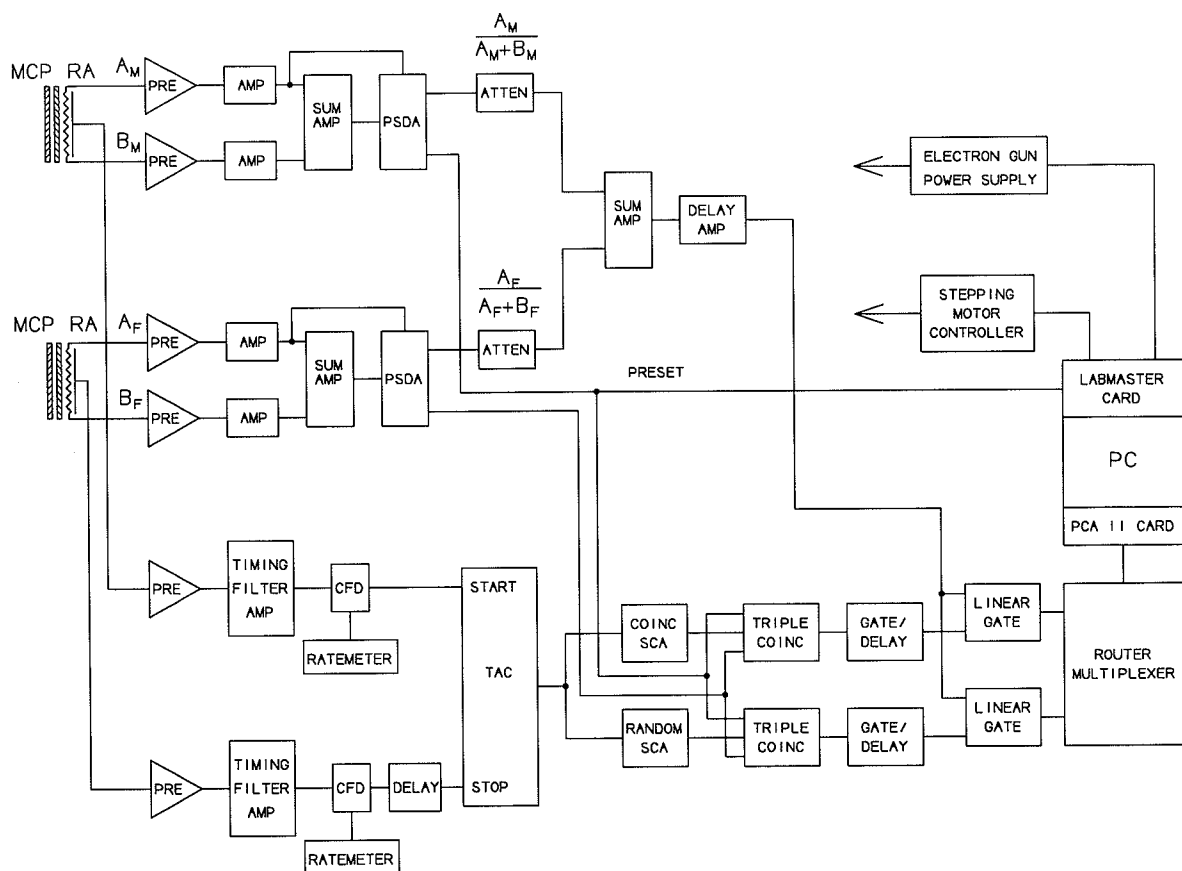
Fig. 2. Schematic diagram of the position sensitive detectors (PSD) and the associated electronics. The PSDs consist of chevron mounted microchannel plates (MCP) and resistive anodes (RA). PSDA, position sensitive detector analyser; CFD, constant fraction discriminator; TAC, time-to-amplitude converter; SCA, single channel analyser; PCA, personal computer analyser (analogue to digital converter card). For details see text.

tional signals from the PSDA are gated by pulses from the true and random SCAs respectively. The two outputs of the linear gates are then digitized in a MCA (personal computer analyser (PCAII) type, Nucleus). A spectrum of true (e, 2e) coincident events alone is derived by subtraction of the random background from the total coincident signal spectrum.

In the present non-coplanar symmetric EMS experiment the energy range of each analyser is set at 600 ± 4.0 eV. The summed-energy range is then from 1192 to 1208 eV for the two outgoing electrons. A flat response function and a good energy linearity across the 8.0 eV range of each detector have been achieved by carefully tuning the electron optics in the lens system and the analyser and detector voltages. The convolution of the square response functions (i.e. a flat distribution over the 8.0 eV energy range and zero elsewhere) of the two analysers results in a triangular response function over the summed-energy range. The method for collecting a coincidence binding energy spectrum with the triangular response function is referred to as the "non-binning" mode. Figs. 3a and 3b show the non-binning coincidence binding energy spectrum of the argon 3p electron and the triangular response function collected in the signal and background windows respectively. Using this data accumulation mode the collected energy spectrum is superimposed on the triangular background and all data points have different detection efficiency, higher in the top region of the triangle and lower near the two ends. This mode is
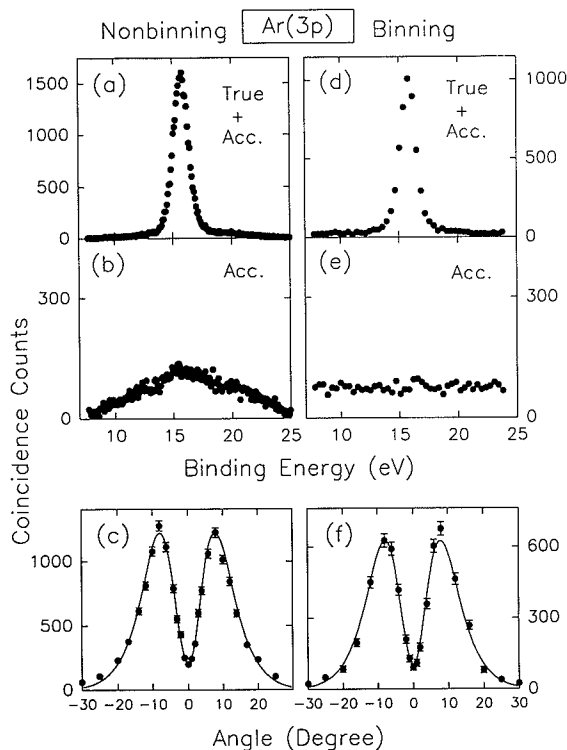
Fig. 3. EMS experiment for the 3p ionization of argon at a total energy of 1200 eV. *Non-binning mode*: (a) the binding energy spectrum collected in the coincidence window, (b) the triangular response function accumulated in the background window, and (c) the angular distribution of the non-binning binding energy spectrum in (a) and the solid line is the calculation for the argon 3p angular profile using the many-body CI wavefunction [30] and the GW-PG resolution folding method [31] with $\Delta\theta = 0.6$ and $\Delta\phi = 1.2$. *Binning mode*: (d) the binding energy spectrum collected in the coincidence window, (e) the flat response function accumulated in the background window, and (f) the angular distribution of the binning binding energy spectrum in (d) and the solid line is the same calculation as in (c).

useful for the more rapid study of a single, well separated binding energy peak such as the HOMO of acetone.

An alternative method for collecting binding energy spectra with a flat overall response function and over a larger energy region is the energy "binning" mode. In this mode the energy range of the detector and the binding energy range to be measured are divided into a number of energy bins corresponding to small equal energy intervals [29]. The interval of the energy bins is set to be 0.36 eV in the present experiment. The coincidence counts in the detector bins are transferred

one by one to the energy bins in the whole energy spectrum as the incident electron beam energy is scanned over the binding energy range in steps of one energy bin. The process of dividing the energy bins and scanning the incident electron beam energy is controlled by a digital-to-analogue converter on the Labmaster board (see Fig. 2) and data accumulation software. Using the energy binning mode each part of the spectrum is collected for an equal number of the preset pulses on each part of the detector so that a uniform detection efficiency or a flat response function over the spectrum is obtained. The triangular detection efficiency involved in the non-binning mode and any local gain variation of the detector are averaged out in the binning mode. Fig. 3d shows the binning coincidence binding energy spectrum of the argon 3p electron and the corresponding flat response function collected in the background (accidental) window is shown in Fig. 3e.

It should be noted that in order to have a given number of bins, all treated in an identical manner, the accumulating program must spend a significant amount of time acquiring data at the ends of the desired range of the binding energy spectrum. As a result the accumulation efficiency of the binning method is much less than that of the non-binning mode particularly for a small energy range of the spectrum.

The ϕ angular distributions for the argon 3p electron collected using both the non-binning and binning modes, are shown in Figs. 3c and 3f respectively. Those two sets of experimental data are remarkably consistent and also show the required symmetry around $\phi = 0°$. The results show good agreement with the argon 3p angular distribution calculated using a many-body CI wavefunction [30]. The finite angular spread of $\Delta\theta = 0.6°$ and $\Delta\phi = 1.2°$, giving a momentum resolution of ~ 0.1 au FWHM for 1200 eV total energy, is folded into the calculation using the GW-PG resolution folding method [31]. The overall energy resolution of the spectrometer due to the energy spread of the incident electron beam and the two hemispherical analysers was measured to be 1.4 eV FWHM using the helium 1s binding energy spectrum.

By using the position sensitive detectors all coincident electrons arriving at the exit planes of the hemispherical analysers can simultaneously be detected giving a spectrum corresponding to a range of binding energies at a given ϕ (i.e. momentum). Data obtained
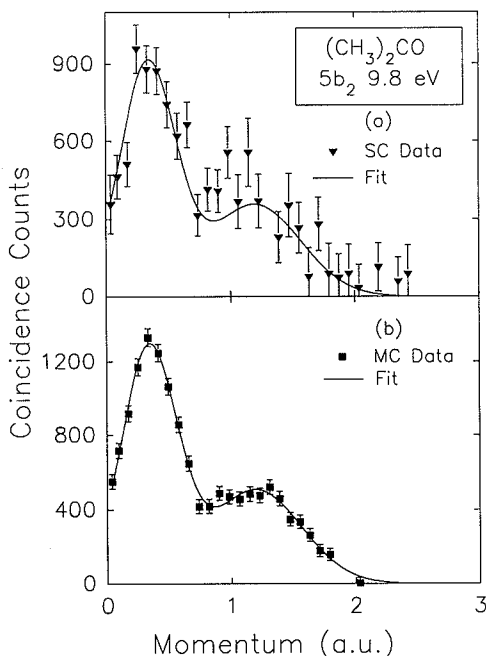
Fig. 4. The measured momentum distributions of the HOMO ($5b_2$) orbital of acetone, (a) by a single channel EMS spectrometer [15], and (b) by the present multichannel EMS spectrometer. The solid lines are a fit to the multichannel experimental data. For details see text.

over a range of ϕ values can thus be reassembled to give a series of orbital momentum distributions. Thus, use of the position sensitive detectors is expected to provide a significant increase in the rate of data accumulation over single channel instruments. For example the momentum distribution of the HOMO ($5b_2$) orbital of acetone, measured using the multichannel EMS spectrometer in the non-binning mode, is compared in Fig. 4 with the earlier result from a single channel spectrometer [15]. It is obvious that the multichannel spectrometer provides much more accurate data. It should be noted that the single channel data (measuring time, 4 weeks) in Fig. 4a would have to be accumulated for ~20 times longer (i.e. > 1.5 years) to obtain equivalent statistics to these in the multichannel spectrum (measuring time, 2 weeks) shown in Fig. 4b.

3. Theoretical considerations

3.1. Theory of electron momentum spectroscopy

The theory and method of electron momentum spectroscopy have been reviewed extensively in the litera-

ture [1–3,5]. Briefly, an (e, 2e) experiment involves high energy electron impact ionization of the target species and coincident detection of the scattered and ejected electrons under predefined scattering kinematics. Energy and momentum conservation give

$$E_0 = E_1 + E_2 + \epsilon_f , \qquad (1)$$

$$p_0 = p_1 + p_2 + q , \qquad (2)$$

where E_0 and p_0 are the energy and momentum of the incident electron, E_1, E_2, p_1 and p_2 are the energies and momenta of the two outgoing electrons, ϵ_f is the electron separation or binding energy for the final ion state $|\Psi_f^{N-1}\rangle$, and q is the recoil momentum of the ion. In symmetric non-coplanar kinematics (i.,e. $E_1 = E_2$, and $\theta_1 = \theta_2 = \theta = 45°$), the recoil momentum is given by

$$q = [(2p_1 \cos \theta - p_0)^2 + 4p_1^2 \sin^2\theta \sin^2\phi/2]^{1/2} . \qquad (3)$$

In this arrangement the out-of-plane azimuthal angle $\phi = \phi_1 - \phi_2 - \pi$ is varied in order to vary the momentum q.

In this kinematic arrangement the momentum transfer ($K = |p_0 - p_1|$) for the collision is large. When the incident electron energy E_0 is high the incoming and two outgoing electrons can be described by plane wave functions, and the ion recoil momentum q is equal and opposite to the momentum p of the ejected electron at the time of the collision. In the plane wave impulse approximation (PWIA) and within the Born–Oppenheimer approximation, the (e, 2e) differential cross section for randomly oriented molecules is given by [1,3]

$$\sigma(e, 2e) = Cf_{ee} \int d\hat{p} \, |\langle p \, \Psi_f^{N-1} | \Psi_i^N \rangle|^2 , \qquad (4)$$

where the spherical average over momentum space is due to the sum over initial rotational states, and the sum over initial vibrational states is represented by evaluating the overlap integral at the equilibrium nuclear distances [1,3]. The quantities C, which is a kinematic factor, and f_{ee}, which is the antisymmetrized electron–electron collision (Mott) cross section, have been shown to be effectively constant within the used range of relative azimuthal angles ϕ under symmetric non-coplanar kinematic conditions [1]. $|\Psi_f^{N-1}\rangle$ and $|\Psi_i^N\rangle$ are the final ion and initial molecule many-body wavefunctions. Thus the (e, 2e) cross section is essentially proportional to the spherically averaged square of the momentum space overlap between the initial

target and final ion states. If the target can be described reasonably accurately by the Hartree–Fock approximation (THFA), which is generally the case for closed shell molecules, then it is a good approximation to replace the many-body wavefunctions $| \Psi_i^N \rangle$ and $| \Psi_f^{N-1} \rangle$ by the independent particle determinants of target Hartree–Fock orbitals. In the THFA, the expression for the (e, 2e) cross section then reduces to [1,3]

$$\sigma(e, 2e) = Cf_{ee} n_j S_j^f \int d\hat{p} \, | \phi_j(p) |^2$$

$$= Cf_{ee} n_j S_j^f F(p) , \qquad (5)$$

where n_j is the occupancy of orbital j and the spectroscopic factor or pole strength S_j^f is the probability that the ion state consists of a hole in the initial state molecular orbital $\phi(p)$. In the THFA the spectroscopic factor is independent of p and satisfies the sum rule

$$\sum_j S_j^f = 1 . \qquad (6)$$

Thus, relative cross sections for different transitions can be used to obtain relative spectroscopic factors (Eq. (5)). The relative cross sections for different orbitals can be normalized if the measured cross sections are summed over all final ion states belonging to a characteristic orbital (Eq. (6)). $F(p)$ is usually called the one-electron momentum profile, which is the spherical average of the square of the momentum-space representation of a single-particle orbital belonging to the symmetry manifold j. The momentum-space wavefunction $\phi_j(p)$ is related to the position-space wavefunction $\psi_j(r)$ by the Fourier transform, i.e.

$$\phi_j(p) = (2\pi)^{-3/2} \int d\hat{r} e^{-ip \cdot r} \psi_j(r) . \qquad (7)$$

3.2. Computational methods

Spherically averaged theoretical momentum profiles (TMPs) of the valence orbitals of acetone have been calculated using the THFA and Eq. (5) with several basis sets, ranging from the minimal basis to the near-Hartree–Fock limit, and also using DFT in the TKSA with the local-density approximation and large atomic natural orbital (ANO) basis sets. The effects of electron correlation and relaxation have been also investigated by calculating the multi-reference singles and doubles excitations configuration interaction (MRSD-

CI) many-body wavefunctions and the ion-neutral overlap distribution (OVD) using Eq. (4) for the HOMO ($5b_2$) and $2b_1$ orbitals. The TMPs include momentum resolution folding using the GW-PG method [31] and can therefore be compared directly with the experimental momentum profiles (XMPs).

The experimental molecular geometry of acetone is obtained from the zero-point vibrationally averaged structure measured by both electron diffraction and microwave rotational spectroscopy [32,33]. However the orientation of the freely rotating methyl groups was not determined in those studies. In the present calculations the methyl geometries were chosen to be in a "half-staggered" conformation (one methyl eclipsed, the other anti to the C=O bond). A theoretical study has been also performed to find out the optimized molecular geometry using the 6-31G** basis set and Hartree–Fock second-order Møller–Plesset perturbation theory (MP2) [15]. Three conformers were found to have minimum energies. They are the "eclipsed" form with both in-plane C–H bonds eclipsed with the C=O bond, the "staggered" form with the in-plane bonds anti to the C=O bond and the "half-staggered" form with one C–H bond eclipsed and one anti. It has been found in the experiment of dimethyl ether that the orientation of the methyl groups has almost no effect on the spherically averaged momentum profiles [12,13]. Some calculations have been also performed for acetone using both the experimental and theoretical molecular geometries and it was found that the difference in the momentum distributions obtained using the experimental and theoretical geometries is negligible. In the present study of acetone the experimental molecular geometry has been used for all of the calculations except for the near-Hartree–Fock limit SCF and subsequent MRSD-CI calculations, for which the "eclipsed" theoretical geometry was used.

The basis sets and methods used for the SCF, TKSA-DFT and MRSD-CI calculations of the valence orbital momentum distributions of acetone are described briefly below and in Table 1. The total energies and dipole moments of acetone predicted by these various calculations are also listed in Table 1.

3.2.1. Basis sets for SCF calculations

(1) STO-3G. A minimal basis set, effectively of single zeta quality, using a single contraction of three Gaussian functions for each basis function. A basis set

Table 1
Basis sets and calculated properties for acetone

Basis type	Reference	Basis set [O, C]/[H]	Total energy (hartree)	Dipole moment (D)
STO-3G	[34]	Gaussian [2s1p]/[1s]	−189.534	1.91
4-31G	[35]	Gaussian [3s2p]/[2s]	−191.676	3.53
6-311G	[36]	Gaussian [4s3p]/[3s]	−191.917	3.56
6-311 + +G**	[36]	Gaussian [5s4p1d]/[4s1p]	−192.014	3.48
204-GTO	[15]	Gaussian [6s7p2d]/[5s1p]	−192.043	3.51
DFT-[543f]	[18]	ANO [5s4p4d]/[4s4p] [a]	−191.599 [b]	3.15
204-G(CI)	[15]	Gaussian [6s7p2d]/[5s1p]	−192.629	3.29
experimental	[48]			2.90 [c]

[a] In this Gaussian type basis set f refers to field induced polarization functions – see text for further details.
[b] The DFT total energy is expected to be shifted from the true value. See Ref. [49] and [18] for details.
[c] In comparing with experimental value of the dipole moment it should be noted that the calculations are at the equilibrium geometry (i.e. for a non-vibrating and non-rotating molecule).

of [2s1p] is used for both oxygen and carbon atoms and [1s] for hydrogen atoms. This basis was designed by Pople and co-workers [34].

(2) *4-31G.* This is a split valence basis which has minimal, single function description of the O and C 1s cores and essentially a double zeta description of the valence shell. It was developed by Ditchfield et al. [35].

(3) *6-311G.* This is also a split valence basis and it comprises an inner shell of six s-type Gaussians, and an outer valence region, which has been split into three parts, represented by three, one and one primitives, respectively. A detailed description of this basis can be found in Ref. [36].

(4) *6-311 + +G**.* Based on the 6-311G basis very diffuse s- and p-functions are added to both oxygen and carbon atoms and diffuse s-functions are added to hydrogen atoms. In addition, polarization functions are also included in the basis, a single set of five d-type Gaussian functions for O and C atoms and a single set of uncontracted p-type Gaussian functions for H atoms [36].

(5) *204-GTO.* These extensive and highly converged Gaussian basis sets reported earlier [15] are based on the work of Partridge [37]. The basis set on the O and C atoms is a (18s13p2d)/[6s7p2d] contracted basis set and the (10s1p)/[5s1p] contracted basis set is used for the H atoms. It should be noted that the 204-GTO and 204-G(CI) treatments were incorrectly referred to as 196-GTO and 196-G(CI) respectively in Ref. [15].

3.2.2. Kohn–Sham DFT calculations

DFT-[543f]. The TKSA-DFT orbital momentum profiles were obtained by performing a Fourier transform of the Kohn–Sham orbitals of the neutral acetone molecule. A detailed description of the method used for the TKSA-DFT calculations can be found elsewhere [18,23]. The Kohn–Sham orbitals were calculated using density functional theory with the local-density approximation and large ANO basis sets [38]. Two types of basis functions, the auxiliary functions for fitting the charge density and exchange–correlation potential and the orbital basis functions for normal LCAO-MO expansion, were used for the TKSA calculations. The auxiliary and orbital basis functions were (5,4;5,4) and [543f] for both O and C atoms, and (4,1;4,1) and [430f] for H atoms. The "f" in the basis set symbol refers to an extra field induced polarization function (consisting of a d-function for C and O atoms and a p-function for H atoms) which has been added to the ANO basis set. It should be noted that the DFT vertical ionization potentials of acetone shown in Table 2 were calculated using the restricted diffuse ionization (RDI) method [39], in which 0.5 electron is removed evenly over all the twelve valence molecular orbitals. The same auxiliary and orbital basis functions used for calculating the TKSA-DFT momentum distributions were also employed in the RDI calculations.

3.2.3. MRSD-CI calculations

204-G(CI). The molecular wavefunctions for both the neutral and ion of acetone were obtained using the multireference singles and doubles configuration interaction (MRSD-CI) method as described in Ref. [15], and then the TMPs were calculated according to the OVD (Dyson orbital) in Eq. (4). The 204-GTO basis set (incorrectly described as 196-GTO in Ref. [15]) used for the near-Hartree–Fock limit SCF calculations was applied for calculating the 204-G(CI) wavefunctions. The frozen core approximation was used in these many-body calculations. This allows for the most detailed description of the valence electrons and the most accurate reproduction of electronic properties possible at the current level of computation [40].

4. Results and discussion

Acetone is a 32-electron molecule and it has C_s symmetry. In simple molecular orbital (MO) theory, the ground state electronic configuration can be written as:

$$(\text{Core})^8 \underbrace{(4a_1)^2 (5a_1)^2 (2b_2)^2}_{\text{Inner-valence}}$$

$$\underbrace{(6a_1)^2 (3b_2)^2 (7a_1)^2 (1b_1)^2 (1a_2)^2 (8a_1)^2 (4b_2)^2 (2b_1)^2 (5b_2)^2}_{\text{Outer-valence}}$$

The inner valence region consists of two a orbitals and one b orbital. There are four a orbitals and five b orbitals in the outer valence region.

4.1. Binding energy spectra

Binding energy spectra of acetone in the range 6–60 eV are shown in Fig. 5. Fig. 5a shows the binding energy spectrum at $\phi = 0°$ and it is dominated by symmetric "s-type" orbitals. In contrast, the binding energy spectrum shown in Fig. 5b illustrates the dominance of "p-type" orbitals, which are anti-symmetric in position space and hence have a minimum at $\phi = 0°$. Gaussian deconvolution is used to separate transitions due to different ionic states. The Gaussian widths are a combination of the instrumental width of the EMS spectrometer and respective Franck–Condon widths. The energy positions and Franck–Condon widths of the outer valence orbitals and the $2b_2$ and $5a_1$ orbitals in the innervalence region are taken from high resolu-
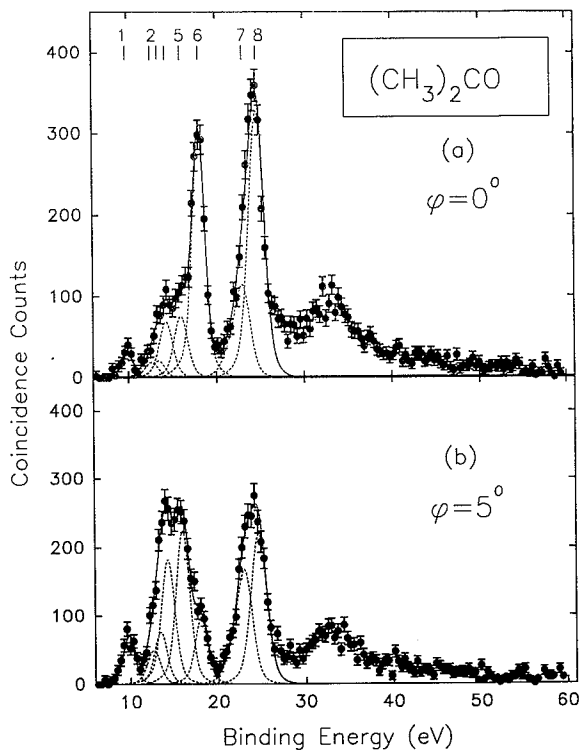

Fig. 5. Valence shell binding energy spectra of acetone from 6 eV to 60 eV at a total energy of 1200 eV. (a) For $\phi = 0°$ and (b) for $\phi = 5°$. The peak numbers 1–8 marked along the top of (a) correspond to ionization from the $5b_2$, $2b_1$, $4b_2$, $(8a_1 + 1a_2)$, $(7a_1 + 3b_2 + 1b_1)$, $6a_1$, $2b_2$, and $5a_1$ orbitals respectively. Gaussian fitting of the experimental data is indicated by the solid lines, and the dashed lines represent individual Gaussians corresponding to the various valence orbitals. The energy positions and Franck–Condon widths are taken from PES studies [24,41]. The Gaussian widths are a combination of the instrumental width of the EMS spectrometer and respective Franck–Condon widths.

tion PES studies [24,41]. The energy spacing and width of the Gaussians are fixed in the fitting procedure. The innervalence $4a_1$ region is not fitted since there are no PES data reported for this orbital and it is not clear what energy positions and widths should be used to fit the broad structure in the 30–38 eV energy range of the EMS spectra. The fitted Gaussians for each peak are indicated by dashed lines and the corresponding peak positions are marked with numbers on the top of Fig. 5a while their sums, the overall fitted spectra, are represented by solid lines.

The calculated and experimental ionization potentials for the different orbitals of acetone are given in Table 2. The HOMO ($5b_2$) and $2b_1$ ionizations peak at

Table 2
Experimental and theoretical ionization potentials (eV) and pole strengths (in parentheses) for acetone

Peak [a]	Orbital	Experiment		Theory			
		EMS	PES [b]	SCF		DFT-[543f] [c]	GF [b]
				6-311++G**	204-GTO		
1	$5b_2$	9.8	9.8	11.305	11.304	9.501	9.85(0.91)
2	$2b_1$	12.6	12.6	13.335	13.191	12.363	12.65(0.90)
3	$4b_2$	13.4	13.4	14.501	14.643	12.705	13.45(0.93)
4	$8a_1$	14.3	14.1	15.188	15.313	13.241	14.05(0.92)
4	$1a_2$	14.3	14.4	15.284	15.322	13.361	14.40(0.93)
5	$7a_1$	16.0	15.7	17.307	17.334	14.680	15.66(0.91)
5	$3b_2$	16.0	15.7	17.526	17.528	14.992	15.93(0.89)
5	$1b_1$	16.0	16.0	16.965	17.002	15.051	16.08(0.92)
6	$6a_1$	18.0	18.0	20.216	20.218	16.656	18.21(0.90)
7	$2b_2$	23.0	23.0	26.246	26.383	21.119	23.78(0.45)
							24.76(0.37)
							26.04(0.021)
8	$5a_1$	24.6	24.6	28.291	28.433	22.751	25.42(0.13)
							25.56(0.043)
							25.60(0.13)
							25.89(0.12)
							26.06(0.27)
							26.30(0.096)
	$4a_1$			37.794	37.473	29.723	29.36(0.024)
							33.32(0.032)
							33.51(0.052)
							33.59(0.032)
							33.63(0.044)
							33.73(0.022)
							33.79(0.021)
							34.94(0.022)
							35.30(0.023)
							36.25(0.052)
							36.44(0.036)
							36.60(0.027)
							36.71(0.038)
							36.76(0.060)
							36.94(0.026)
							41.38(0.027)

[a] See Fig. 5 and text.
[b] The OVGF and the extended 2ph-TDA methods were used for the outer- and inner-valence ($2b_2$, $5a_1$ and $4a_1$) orbitals respectively, using a (9s5p/4s)/[4s2p/2s] limited basis set, see Ref. [24] and text for details.
[c] The restricted diffuse ionization method was used, for details see Ref. [39].

9.8 and 12.6 eV respectively. The measured EMS IPs of these two orbitals are consistent (Table 2) with the high resolution PES data from Ref. [24]. The HOMO (peak 1) is well resolved in the EMS binding energy spectra. The HOMO is mainly due to the lone-pair 2p electrons of the oxygen atom and the $2b_1$ orbital (peak 2) has C=O π character. The third outer valence

orbital, $4b_2$ (peak 3 located at 13.4 eV), is primarily due to C–H σ bonding. The $8a_1$ and $1a_2$ peaks are not well resolved in the PES spectrum [24] and their IPs are approximately 14.1 and 14.4 eV respectively. In the lower resolution EMS data peak 4 at 14.3 eV involves ionization from both of these orbitals. Similarly the next three outer valence orbitals, the $7a_1$, $3b_2$

and $1b_1$ orbitals, have very closely spaced IPs and their PES binding energies are 15.7, 15.7 and 16.0 eV respectively. A peak at 16.0 eV (peak 5) is therefore fitted to the EMS binding energy spectra for these three orbitals. The assignment of ionization potentials of these closely spaced orbitals is still controversial. For example the $1b_1$ orbital energies predicted by the 6-311 + +G** and 204-GTO calculations are in a different order from the ionization potentials given by the DFT and GF calculations (see Table 2 for details). It is not possible to clarify this issue by studying their angular (ϕ) distributions in the present EMS study due to the close energy spacing of these orbitals. The last outer valence orbital is the $6a_1$ at 18.0 eV (peak 6).

The PES IPs of the first two innervalence orbitals, i.e. the $2b_2$ and $5a_1$ orbitals, are 23.0 (peak 7) and 24.6 (peak 8) eV respectively [24]. However there are no experimental PES data for the $4a_1$ orbital. In the inner-valence region of 28–60 eV there is obviously significant splitting of the ionization lines due to strong electron correlation effects. A broad peak in the energy range of 30–38 eV can be seen in the EMS binding energy spectra in Fig. 5 and the ionization strength is further spread over a large range of binding energies up to 60 eV with no apparent peak structures. The Green's function calculation [24] predicts considerable splitting of each of the three innervalence orbitals. The calculated energy poles and pole strengths are given in Table 2. It can be seen from the EMS binding energy spectra in Figs. 5a and 5b that the intensity in the 28–60 eV region is larger at $\phi=0°$ than that at $\phi=5°$. It can therefore be concluded that the $5a_1$ and $4a_1$ manifolds (symmetric) dominate in this energy region. Further discussion of the angular distributions of the two manifolds is given below.

Calculated binding energy spectra are compared with the measured binding energy spectra in Fig. 6. The synthesized spectra are obtained by using the pole energies and pole strengths given by the Green's function calculation [24] in Table 2, and the 204-GTO SCF wavefunction to calculate the momentum distribution (and thus the ϕ angle dependence) at each binding energy using Eq. (5). The measured EMS instrumental energy resolution function, as well as the widths of the transitions as observed in high resolution PES [24], have been folded into the calculated spectra. The width of the $5a_1$ peak has also been used for the $4a_1$ poles in the synthesized spectra since there are no PES data
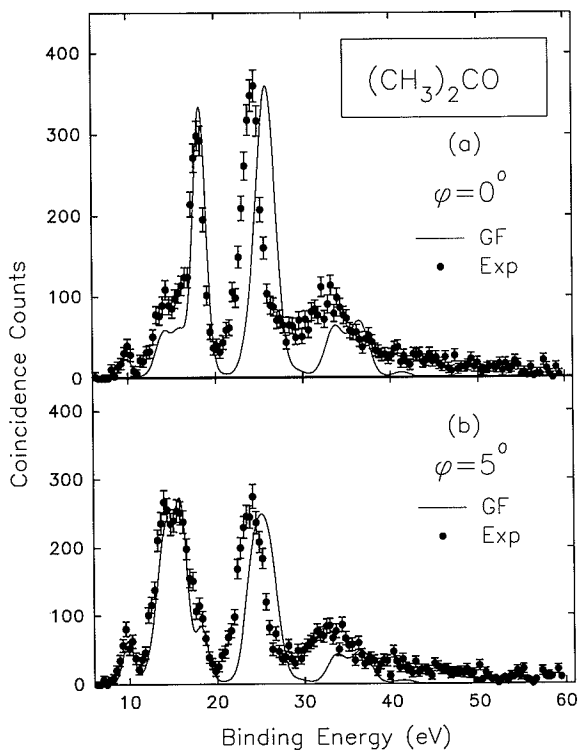

Fig. 6. Measured and calculated binding energy spectra of acetone from 6 to 60 eV at (a) $\phi=0°$ and (b) $\phi=5°$. The solid curves indicate the synthesized theoretical binding energy spectra with pole energies and pole strengths (Table 2) given by the limited basis set Green's function many-body calculations [24]. The angular dependence is determined from the near-Hartree–Fock limit SCF wavefunction (204-GTO). The same energy peak widths as used in Fig. 5 have been folded into the synthesized spectra. See text for details.

reported for this process. Agreement between experiment and theory is good in the outer valence region of the spectra. The measured intensity at the lower momentum ($\phi=0°$) is slightly underestimated and this is consistent with the comparison of the measured and calculated momentum profiles presented in the next subsection. In the innervalence region, the calculated energy positions for the $2b_2$, $5a_1$ and $4a_1$ main peaks are shifted by 1–2 eV in comparison to the experimental spectra. The strength of the $2b_2$ and $5a_1$ main peaks is well described by the calculations. However, the measured strengths in the 30–60 eV energy regions are underestimated by the theoretical calculations. This discrepancy could be due to either the inadequacy of the Green's function calculations or the SCF wavefunctions. However, since the near Hartree–Fock limit

SCF wavefunction (204-GTO) gives a good description in both shape and intensity of momentum distributions of those innervalence orbitals of acetone (see next subsection for the comparison of the momentum distributions) it is likely that the discrepancies are mainly due to the intermediate quality basis set and 2ph-TDA innervalence approximation used in the Green's function calculations [24].

4.2. Experimental and theoretical momentum distributions

Experimental and theoretical spherically averaged momentum profiles have been obtained for the valence orbitals of acetone. Experimental momentum distributions are extracted from the sequentially obtained, angular-correlated, multichannel (binning mode) binding energy spectra, and therefore the relative normalizations for the different transitions are maintained. The Gaussian fitting procedure, described above for the binding energy spectra, is used to determine the relative intensities of the various transitions at each azimuthal angle ϕ. The experimental momentum distribution for a particular transition is obtained by plotting the area under the corresponding fitted peak for each electronic state of the ion as a function of p (i.e. ϕ angle). With this procedure all momentum distributions are automatically placed on the same relative intensity scale. The various theoretical momentum profiles (TMPs) of the valence orbitals are obtained as described in Section 3. The experimental finite momentum resolution ($\Delta p \sim 0.1$ au), obtained by fitting the measured angular distribution of the argon 3p state, shown in Figs. 3c and 3f, is also folded into the TMPs using the GW-PG method [31].

The experimental and theoretical momentum distributions have been placed on a common intensity scale by normalizing the experimental data, summed from 6 to 20 eV, to the SCF momentum distributions calculated using the 204-GTO basis sets and summed over the nine outervalence orbitals in Fig. 7a. The reasons for choosing this normalization are that the 204-GTO results are high level SCF calculations (near-Hartree–Fock limit) and the shapes of the summed 204-GTO calculations and measured momentum distributions of the outervalence orbitals are in reasonably good agreement (Fig. 7a). The pole strengths of these transitions in the outervalence region are also high from the many-
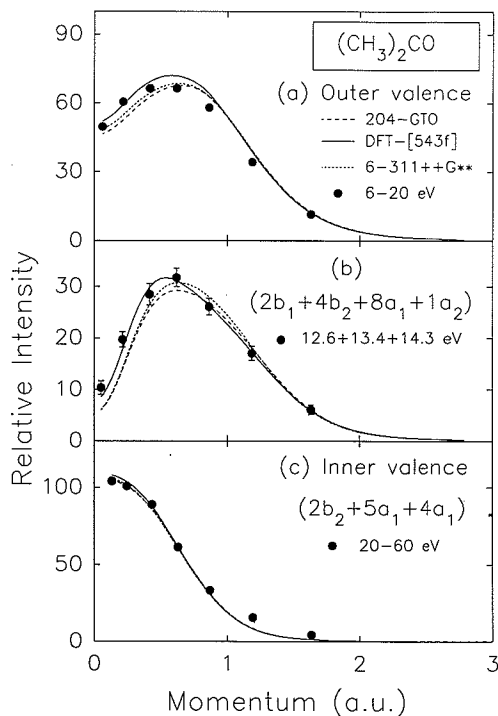

Fig. 7. Summed experimental and calculated spherically averaged momentum distributions of the outer-valence and inner-valence orbitals of acetone. (a) The experimental data points are obtained by summing the measured binding energy spectra from 6 to 20 eV over the azimuthal angles (momentum). The solid curve is the sum of the momentum distributions calculated by the TKSA-DFT method for all nine outer-valence orbitals ($5b_2$, $2b_1$, $4b_2$, ($8a_1 + 1a_2$), ($7a_1 + 3b_2 + 1b_1$), and $6a_1$), the long dashed curve represents the summed momentum distributions predicted by the near-Hartree–Fock limit SCF wavefunction (204-GTO), and the short dashed line is the sum of the 6-311 + +G** SCF calculations. (b) The summed experimental data for the intensities of the peaks at 12.6, 13.4 and 14.3 eV is compared with the sum of the calculations for the $2b_1$, $4b_2$ and $8a_1 + 1a_2$ orbitals. (c) The summed experimental data in the inner-valence region (20–60 eV) is compared with the sum of the calculated momentum distributions for the $2b_2$, $5a_1$ and $4a_1$ orbitals. The momentum resolution has been folded into all calculations using the GW-PG method [31] and the data are normalized as explained in the text.

body Green's function calculations [24] (see Table 2). The same normalization factor obtained in this procedure is then used for each individual orbital for all experimental and theoretical comparisons.

The theoretical and experimental momentum distributions of all the valence orbitals of acetone are presented in Fig. 8 using the above normalization. In the
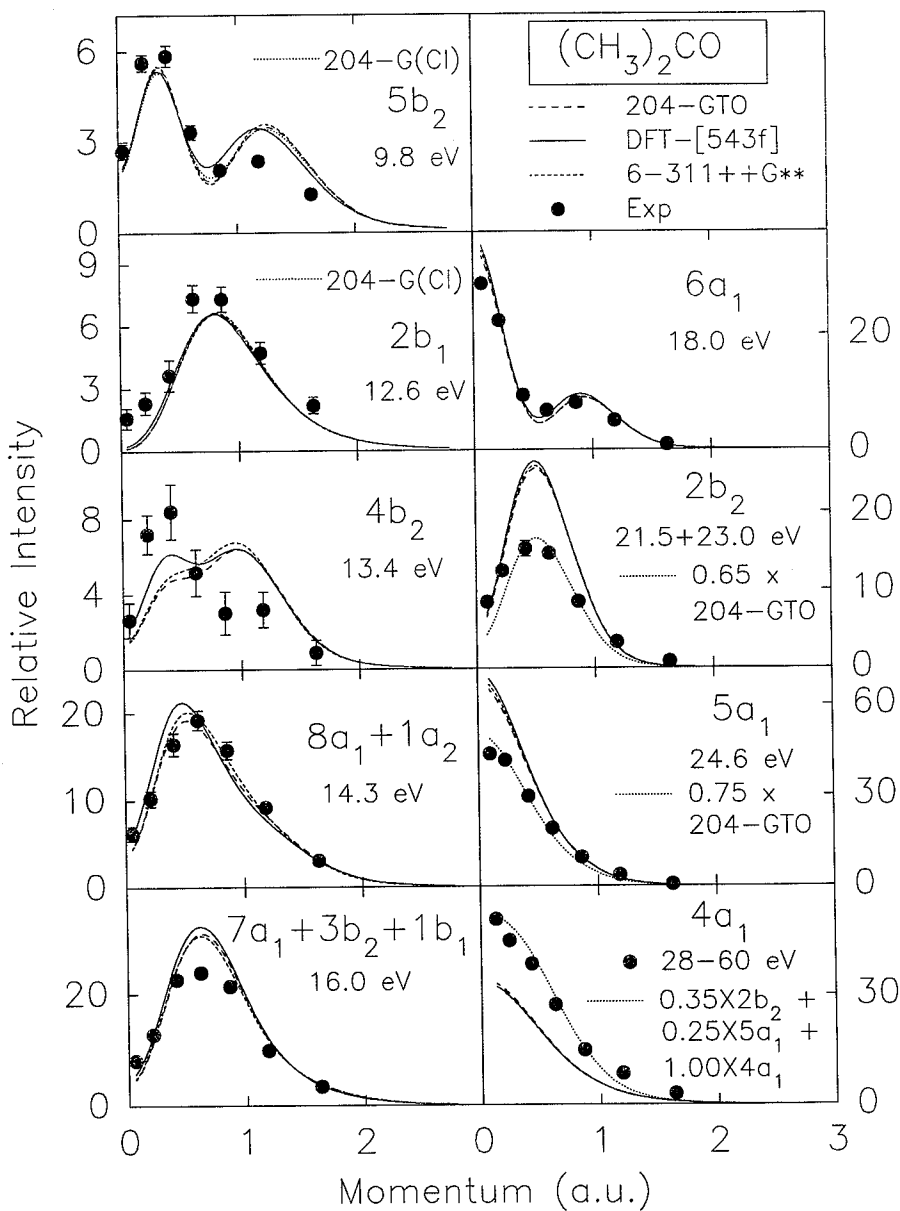
Fig. 8. Spherically averaged experimental and theoretical momentum distributions for all the valence orbitals of acetone. The solid dots are the experimental data obtained by deconvoluting the corresponding peaks from the binding energy spectra of various ϕ angles. The theoretical momentum distributions represented by solid, long dashed and short dashed lines are calculated using the TKSA-DFT method (DFT-[543f]), 204-GTO SCF and 6-311+ +G** SCF wavefunctions respectively. The calculations using the MRSD-CI method (204-G(CI)) are also given for the $5b_2$ and $2b_1$ orbitals, represented by the dotted lines (overlapped with the 204-GTO and the 6-311+ +G** for the $2b_1$ orbital). The solid dots for the $4a_1$ orbital are the experimental data summed over the 28–60 eV energy range and the dotted line represents the sum of $0.35(2b_2) + 0.25(5a_1) + 1.0(4a_1)$ of the 204-GTO SCF calculation. The momentum resolution has been folded into all calculations using the GW-PG method [31] and the same normalization factor is used as in Fig. 7. For details see text.
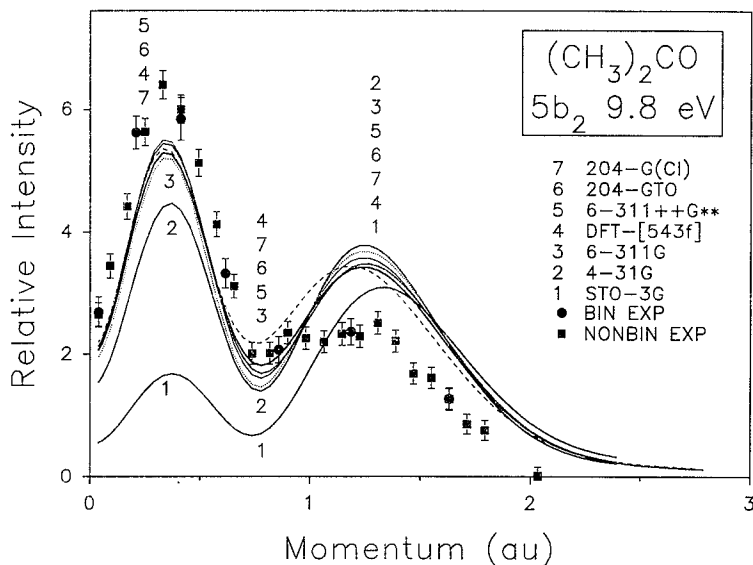
Fig. 9. Measured and calculated spherically averaged momentum distributions for the $5b_2$ HOMO orbital of acetone. The solid square points are the experimental data collected using the non-binning data accumulation mode as shown in Fig. 4b. The solid circular points are the measured data from Fig. 8 for this orbital obtained using the energy binning mode. In addition to the four calculations, i.e. DFT-[543f], 6-311 + +G** SCF, 204-GTO SCF and 204-G(CI) given in Fig. 8 three lower level SCF calculations (STO-3G, 4-31G and 6-311G) are also shown for this orbital. The momentum resolution has been folded into all calculations using the GW-PG method [31] and the same normalization factor is used as in Fig. 7.

following discussion the comparison between theory and experiment will be made for each orbital in turn.

4.2.1. The momentum distributions of the HOMO orbital

The frontier molecular orbital theory of Fukui [42] and the work of Woodward and Hoffmann [43] have emphasized the importance of the role of the electron density of the highest-occupied molecular orbital (HOMO) in determining chemical reactivity. Therefore it is important to obtain a detailed understanding of the electronic structure of the HOMO. Although the momentum distribution of the HOMO of acetone has been previously measured using a single channel EMS spectrometer [15] the accuracy and statistics of the experimental data were extremely limited due to the low cross section of this orbital (see Fig. 4a). The momentum distribution of the HOMO shows a double peak distribution. In particular the single channel data exhibits a large uncertainty for both the peak position and intensity in the case of the second peak. In the present work in addition to the "binning" experiment for all the valence orbitals of acetone, as shown in Fig.

8, an independent experiment has been also carried out for the HOMO orbital by using the non-binning data accumulation mode. In the latter experiment data were collected at twenty-four ϕ angles in order to have a sufficient density of momentum data points over the 0–3 au momentum range. Fig. 9 shows the non-binning experimental data along with the data obtained in the binning mode (as shown previously in Fig. 8). It can be seen from Fig. 9 that the two sets of experimental data from the non-binning and binning modes are remarkably consistent. Various calculations are compared in Fig. 9 with these experimental data and the same normalization factor as in Fig. 8 is used.

The HOMO of acetone is mainly due to the lone-pair oxygen 2p electrons, but with a large contribution also from the methyl group carbons and the methyl group hydrogens. These methyl C–H σ bonds introduce an additional nodal surface in the electron charge density and result in a local minimum in the momentum distribution for this orbital. The experimental data shows a double "lobed" momentum distribution with peaks at about 0.33 and 1.15 au respectively. Seven calculations shown in Fig. 9 are compared with the

experimental data and all predict a double peak momentum distribution for this orbital. The comparison between experiment and theory shows that a continuous improvement occurs in the fit to the first peak of the experimental data as the basis set is successively enlarged from STO-3G to 4-31G and 6-311G. The STO-3G calculation predicts a greater intensity for the second peak than the first peak in the momentum distribution and this is obviously in disagreement with the experimental data. The 4-31G and 6-311G calculations give a much better description than the STO-3G model. The predicted peak positions for both "lobes" are shifted towards the experimental positions. The intensity ratio of the first peak to the second peak is increased for the 4-31G and 6-311G calculations and it agrees better with the experimental data. The calculated total energies and dipole moments are also improved as the basis set is enlarged (see Table 1).

An improved agreement with the experimental data can be seen from the 6-311 + +G** calculation as the diffuse and polarization functions are added. The diffuse functions with small exponents increase the electron density at long range relative to the density near the nuclei. Since EMS experiments preferentially probe the wavefunction structure in the small p region (which emphasizes the larger r region, see Eq. (7)) diffuse functions can be very important in predicting momentum distributions of molecular orbitals [9]. Intermediate size basis sets with very diffuse functions can result in significantly improved theoretical momentum distributions for outervalence orbitals [44,45]. On the other hand total energies are strongly dependent on the electron density nearer the nucleus and are therefore not very sensitive to the large r effects (see Table 1).

The TKSA momentum distribution, calculated using DFT in the local-density approximation with the large ANO basis sets, is very similar to the 6-311G and 6-311 + +G** calculations in the low momentum region (first peak), but there is a difference in the momentum range higher than 0.5 au. The TKSA-DFT calculation has a higher minimum (at 0.75 au) compared to the other calculations. However the peak position for the second peak predicted by the TKSA-DFT theory is somewhat closer to the experimental data than those calculated by the other models. The near-Hartree–Fock limit SCF wavefunction with the very large and very diffuse basis set (204-GTO) provides a momentum distribution similar to the 6-311 + +G** calculation.

The intensity and peak position of the second peak are still overestimated by this wavefunction as is the case for all the other SCF wavefunctions. The calculation of the ion–neutral overlap including electron correlation and relaxation by using Eq. (4) and the MRSD-CI wavefunction (204-G(CI)) gives a momentum distribution similar to the one calculated by using the near-Hartree–Fock limit SCF wavefunctions. Based upon the above comparison it seems that the effects of electron correlation and relaxation are very small for the momentum distribution of the HOMO of acetone. This result is very different from results obtained for some other molecules, such as H_2O [9], NH_3 [8,9], HF [10] and BF_3 [46], where electron correlation effects significantly affect the momentum distributions of HOMO orbitals, particularly in the low momentum region.

In summary the 6-311G, 6-311 + +G**, 204-GTO SCF and 204-G(CI) wavefunctions and the TKSA-DFT theory give similar descriptions for the momentum distribution of the HOMO in the low momentum range (around the first peak at about 0.33 au). However all the calculations underestimate the ionization intensity in this low momentum range although they correctly predict the position of the first peak with the exception of the STO-3G model. Usually, HOMO orbitals are very diffuse in position space and they contribute the least to the total energy. Therefore, their diffuse outer regions are likely to be less well modelled by the SCF variational method. Thus highly saturated basis sets including very diffuse functions are expected to be necessary in order to produce converged results particularly for HOMO momentum distributions [7–10,46]. In many cases the effects of electron correlation and relaxation are also significant. However in the case of acetone discrepancies remain between experiment and theory in the low momentum range even with the many-body MRSD-CI calculations using large and highly saturated basis sets. Furthermore, none of the calculations provides an adequate description of the second peak of the HOMO momentum distribution in the high momentum range. The calculated intensities are much higher than the experimental data and the peak positions are shifted towards higher momentum except for the peak position predicted by the TKSA-DFT theory. It should also be noted that the discrepancies at higher momentum are in the contrary direction to that expected for distorted wave effects in the experimental data [1–6].

4.2.2. The momentum distributions of the other outer-valence orbitals

The second outermost orbital of acetone is the $2b_1$ peaking at 12.6 eV in the EMS binding energy spectra in Fig. 5. This orbital is primarily due to C=O π bonding. Fig. 8 shows that the momentum distribution of the $2b_1$ orbital is "p-type" with the momentum peak position ~ 0.9 au. The four calculations, from the 6-311++G** and 204-GTO SCF wavefunctions and the 204-G(CI) and TKSA-DFT methods, are compared with the experimental data. All four calculations give a very similar momentum distribution for this orbital. This shows that the electron correlation and relaxation effects included in the many-body CI wavefunctions are not significant for this momentum distribution of acetone, similar to the situation discussed above for the momentum distribution of the HOMO. All the calculations predict the momentum peak position of the $2b_1$ orbital quite well, but the experimental intensity is underestimated by theory below ~ 1 au.

The IP of the $4b_2$ orbital is 13.4 eV. The TKSA-DFT calculation in Fig. 8 predicts a doublepeak momentum distribution for this orbital, peaked at about 0.4 and 1.0 au respectively, with comparable intensities. The 204-GTO and 6-311++G** SCF wavefunctions also give a similar double-peak distribution, but with the ionization intensity of the second peak being considerably higher than that of the first peak. The predicted momentum distributions in the momentum region above 0.8 au are however very similar. In contrast the measured momentum distribution shows a strong peak around 0.4 au and a weaker peak at about 1.0 au. The calculations significantly underestimate the experimental intensity in the low momentum region and overestimate the experimental data in the high momentum range.

The peak at 14.3 eV in the EMS binding energy spectra (Fig. 5) is due to the $8a_1$ and $1a_2$ orbitals. The deconvoluted momentum distribution of this combined peak is shown in Fig. 8 and it has a "p-type" distribution with a maximum at about 0.7 au. According to the calculations the $1a_2$ orbital has a "p-type" distribution and the $8a_1$ orbital has a double-peak momentum distribution with the second peak at about 1.2 au. The tailing in the summed momentum distribution of these two orbitals is therefore mainly due to the second momentum peak of the $8a_1$ orbital. The calculations with the 204-GTO and 6-311++G** SCF wavefunc-

tions describe the peak position and intensity of the experimental data quite well. However, the peak position predicted by the TKSA-DFT theory is slightly shifted towards low momentum. This results in a higher intensity in the low momentum region and a lower intensity in the higher momentum range.

From the above comparison it is obvious that there are discrepancies between experiment and theory for the $2b_1$, $4b_2$ and $(8a_1 + 1a_2)$ orbitals. There could be several sources for these discrepancies such as errors in the deconvolution procedure in the data analysis and the inadequacy of the calculations. These four orbitals have closely spaced binding energies (energy separations less than 1.0 eV) and they are therefore not resolved in the present EMS data (the instrumental width is 1.4 eV FWHM). Therefore it is likely that errors arise in the deconvolution of these overlapping peaks in the data analysis. If the summed experimental data of these four orbitals is compared with the sum of the calculations the deconvolution errors can be eliminated. These ideas are supported by the improved agreement between experiment and theory shown in Fig. 7b where the experimental data summed over these four orbitals are compared with the summed calculations. The comparison shows that the TKSA-DFT theory gives a very good description for the summed experimental data. The calculations with the 204-GTO and 6-311++G** SCF wavefunctions are very similar, but they underestimate the experimental data in the low momentum range from 0 to 0.6 au and slightly overestimate the measured intensity in the high momentum range. This is consistent with the comparison in Fig. 7a which is for all the outervalence orbitals.

The PES binding energies of the $7a_1$, $3b_2$ and $1b_1$ outervalence orbitals are 15.7, 15.7 and 16.0 eV respectively as given in Table 2. These three orbitals are all included in the peak at 16.0 eV in the EMS binding energy spectra in Fig. 5. The summed momentum distribution for these three orbitals, shown in Fig. 8, shows a "p-type" behaviour. The 204-GTO and 6-311++G** results are almost identical while the TKSA-DFT theory gives a slightly higher intensity around the peak region. All the three calculations overestimate the experimental intensity.

The last orbital in the outervalence region is the $6a_1$ which peaks at 18.0 eV in the binding energy spectra (Fig. 5). This orbital has mixed "s–p" symmetry. The intensity at the momentum origin is due to the contri-

bution of the O 2s electrons. The minimum at $p \sim 0.6$ au indicates the antisymmetric overlap between the O 2s component and C 2p component on the carbonyl carbon. The cross section in the region of $p \sim 1.0$ au is mainly from the C 2p electrons. The comparison of the measured momentum distribution with theory in Fig. 8 shows that all three calculations provide a very good description of the peak position and the "s-to-p" ratio.

The comparison between experiment and theory for all nine orbitals in the outervalence region of acetone is shown in Fig. 7a. The three calculations using the 204-GTO and 6-311 + +G** SCF wavefunctions and the TKSA-DFT theory give similar results for the sum of all the outervalence orbitals in the momentum region above 0.9 au. The TKSA-DFT theory predicts a higher intensity in the lower momentum range than the other two calculations. In general, agreement between experiment and theory is reasonably good. The TKSA-DFT theory seems to give a slightly better fit to the experimental data. However, all three calculated momentum distributions peak at slightly higher values of momentum than in the experiment.

4.2.3. The momentum distributions of the innervalence orbitals

Fig. 7c shows the results for the inner valence orbitals with the summed intensity over the energy range of 20–60 eV being compared with the sum of the calculated momentum densities for the $2b_2$, $5a_1$ and $4a_1$ orbitals. This region should contain essentially all of the ionization strength from the three innervalence orbitals. The spectroscopic sum rule (Eq. (6)) can be used to obtain manifold cross sections. The comparison of the summed experimental data with the sum of the calculated momentum distributions over the innervalence region eliminates any errors in the calculated energies of the poles and is only sensitive to the shape of the calculated momentum distributions. It is shown in Fig. 7c that the three calculations using the 6-311 + +G** and 204-GTO SCF wavefunctions and the TKSA-DFT theory are very similar and fit the experimental data very well both for shape and intensity in the momentum region below 1.0 au. The small discrepancy between theory and experiment in the momentum region higher than 1.0 au could be due to distortion of the electron waves [1,3].

The first innervalence orbital is the $2b_2$ orbital. The Green's function calculation predicts the splitting of

this orbital into three poles at 23.78, 24.76 and 26.04 eV (see Table 2). The PES data [24] shows a main peak at 23.0 eV and a very broad tail in the low energy side with considerable intensity. In the present EMS data, in addition to the main peak at 23.0 eV another peak at 21.5 eV is used to fit the experimental data and it is included in the main peak in Fig. 5. The energy width of this peak is the same as the width of the main peak at 23.0 eV. The momentum distribution of this peak is very similar to that of the main peak, having a "p-type" distribution peaked at about 0.5 au. This indicates that the intensity at 21.5 eV is mainly due to the splitting of the $2b_2$ orbital. In Fig. 8 the summed momentum distributions of the two peaks at 21.5 and 23.0 eV are compared with the calculations for the $2b_2$ orbital. The calculations from the 6-311 + +G** and 204-GTO SCF wavefunctions and the TKSA-DFT theory are very similar for this orbital, but all three calculations significantly overestimate the observed intensity. This suggests that some of the transition intensity from this orbital is located in the higher energy range. An estimated pole strength of 0.65 is used to bring the 204-GTO calculation down for shape comparison (the dotted line in Fig. 8). If this is done the experimental data in the low momentum range is underestimated by the calculations. In this case the "extra" intensity observed near the origin could be due to contributing poles from the neighboring $5a_1$ process, which has an "s-type" momentum distribution. It is also possible that errors in the data deconvolution cause some intensity from the $5a_1$ orbital to be included in the momentum distribution of the $2b_2$ orbital.

The high resolution PES data [24] shows that the $5a_1$ orbital has a main peak at 24.6 eV. The Green's function calculation predicts several poles for ionization from this orbital which are distributed over a wide energy range (see Table 2). The $5a_1$ has an "s-type" momentum distribution. The momentum distribution of the main $5a_1$ peak at 24.6 eV is compared with the calculations in Fig. 8. Again, all three calculations, using the 204-GTO and 6-311 + +G** SCF wavefunctions and the TKSA-DFT theory, produce very similar momentum distributions for this orbital. In order to compare the shape of the momentum distribution the 204-GTO calculation is multiplied by an estimated pole strength of 0.75 and the reduced momentum profile is represented by the dotted line in

Fig. 8. An excellent shape agreement between experiment and theory is then obtained.

The EMS binding energy spectra in Fig. 5 indicate that there is significant splitting in the energy region from 28 up to 60 eV. All the $2b_2$, $5a_1$ and $4a_1$ ionization processes in the innervalence region could have a range of poles in this energy region although the Green's function calculations [24] predict only $4a_1$ poles. However there are no clearly defined structures in the measured binding energy spectrum. Therefore the momentum distribution summed over this 28–60 eV energy range is discussed here. The summed experimental data is shown in Fig. 8 and it is dominated by totally symmetric (i.e. "s-type") components. This indicates that the strength over this energy region is mainly from the $5a_1$ and possibly $4a_1$ orbitals since both these orbitals have "s-type" momentum distributions. The Green's function calculation certainly predicts a strong splitting for the $4a_1$ orbital with many poles over this energy range (see Table 2). The calculated momentum distributions for the $4a_1$ orbital are therefore compared with the experimental data in Fig. 8. It is obvious that the observed intensity in this energy region is stronger than the $4a_1$ strength alone. A good fit to the experimental data is obtained when, for example for the 204-GTO SCF calculation, the $2b_2$ and $5a_1$ components with spectroscopic factors of 0.35 and 0.25 respectively are added to the $4a_1$ momentum distribution (see the dotted line in Fig. 8). It is important to note that the factors of 0.35 and 0.25 correspond exactly to the pole strengths predicted to be missing from the main peaks of the $2b_2$ (23.0 eV) and $5a_1$ (24.6 eV) processes respectively, according to the shape matching scaling factors discussed above (see Fig. 8). This analysis is also consistent with the comparison shown in Fig. 7c for the sum of the three innervalence orbital momentum distributions.

5. Conclusions

Using the high sensitivity of the new multichannel EMS spectrometer a study of the entire valence orbital region of acetone has been completed. The experimental data have been analysed and compared with a wide range of calculations. The binding energy spectra in the energy range of 6–60 eV have been compared with the Green's function calculations [24]. In the outer-valence region the Green's function calculations qualitatively describe the energy positions and pole strengths of the binding energy spectra. In the inner-valence region strong splitting of the $2b_2$, $5a_1$ and $4a_1$ orbitals due to final state electron correlation is observed. The distribution of energy poles and pole strengths predicted by the Green's function calculations deviates seriously from the measured ionization energies and strengths. These discrepancies are likely due to the limited basis set and the inadequacy of the 2ph-TDA approximation [24].

The experimental momentum distributions of the complete valence orbitals of acetone have been used to evaluate various theoretical models including SCF wavefunctions ranging from the minimal basis set to the near Hartree–Fock limit, Kohn–Sham DFT calculations using the local-density approximation and large ANO basis sets and many-body MRSD-CI treatments with the large and saturated basis sets. In general, the SCF wavefunctions with the intermediate basis set and very diffuse functions, i.e. $6\text{-}311++G^{**}$, and the near-Hartree–Fock limit SCF and the TKSA-DFT theory predict the momentum distributions of most orbitals reasonably well in the outervalence region. Comparing the two SCF calculations and the TKSA-DFT theory the latter gives a slightly better fit to the experimental data. However, none of the theoretical models adequately describes the momentum distribution of the HOMO. Incorporation of electron correlation and relaxation effects using the large basis set MRSD-CI wavefunctions and the full ion-neutral overlap calculations results in a momentum distribution for this orbital similar to that obtained using the near-Hartree–Fock limit SCF wavefunction. The calculations including electron correlation and large r effects do not significantly improve the theoretical momentum distribution and it appears that even further high level theoretical work may be required for the HOMO of acetone. The shapes of the momentum distributions of the innervalence orbitals are well described by the $6\text{-}311++G^{**}$ SCF, near-Hartree–Fock SCF and the TKSA-DFT calculations.

This EMS experiment for acetone has demonstrated that the rate of data accumulation using the multichannel spectrometer is significantly increased over conventional single channel EMS instruments. The momentum distributions of two closely spaced orbitals, such as the $2b_1$ and $4b_2$ orbitals with separation energy

difference of 0.8 eV, can be obtained by curve fitting multichannel binding energy spectra obtained at a range of azimuthal angles. Therefore, using this type of multichannel EMS spectrometer and the associated techniques for data analysis the experimental difficulties of low volatility and closely spaced orbital energies for larger species such as prototype biological and biochemical molecules can be overcome and EMS experiments on such systems should be possible with suitable sample evaporation techniques [47]. This study has also shown that the Kohn–Sham DFT theoretical model, using the local-density approximation and large ANO basis sets, gives very similar electron momentum distributions for the valence orbitals of acetone to those given by the ab initio near-Hartree–Fock limit SCF and many-body MRSD-CI models. Furthermore it has been found that both TKSA-DFT and high level MRSD-CI ion–neutral overlap method (or near-Hartree–Fock limit SCF where this level of treatment is sufficient) provide very good descriptions of the shapes of the experimental momentum profiles for a range of smaller molecules [18]. With these various perspectives in mind it is therefore of interest in future studies to investigate the application of the Kohn–Sham DFT theory to the calculation of the momentum distributions for even larger molecules.

Acknowledgement

References

[1] I.E. McCarthy and E. Weigold, Phys. Rept. 27 (1976) 275.
[2] C.E. Brion, Intern J. Quantum Chem. 29 (1986) 1397, and references therein.
[3] I.E. McCarthy and E. Weigold, Rept. Prog. Phys. 51 (1988) 299.
[4] I. McCarthy and E. Weigold, Rept. Prog. Phys. 91 (1991) 789, and references therein.
[5] C.E. Brion, in: Correlations and polarization in electronic and atomic collisions and (e, 2e) reactions, Inst. Phys. Conf. Series 122 (1992) 171 (Institute of Physics, Bristol).
[6] C.E. Brion, in: The physics of electronic and atomic collisions, eds. T. Andersen et al. (American Institute of Physics Press, New York, 1993) p. 350.
[7] A.O. Bawagan and C.E. Brion, Chem. Phys. Letters 137 (1987) 573.
[8] A.O. Bawagan, R. Muller-Fiedler, C.E. Brion, E.R. Davidson and C. Boyle, Chem. Phys. 120 (1988) 335.
[9] A.O. Bawagan, C.E. Brion, E.R. Davidson and D. Feller, Chem. Phys. 113 (1987) 19.
[10] B.P. Hollebone, Y. Zheng, C.E. Brion, E.R. Davidson and D. Feller, Chem. Phys. 171 (1993) 303.
[11] E. Weigold, Y. Zheng and W. von Niessen, Chem. Phys. 150 (1991) 405.
[12] S.A.C. Clark, A.O. Bawagan and C.E. Brion, Chem. Phys. 137 (1989) 407.
[13] Y. Zheng, E. Weigold, C.E. Brion and W. von Niessen, J. Elec. Spectry. Relat. Phenom. 53 (1990) 153.
[14] J.J. Neville, Y. Zheng and C.E. Brion, Chem. Phys. (1994), to be published.
[15] B.P. Hollebone, P. Duffy, C.E. Brion, Y. Wang and E.R. Davidson, Chem. Phys. 178 (1994) 25.
[16] Y. Zheng, Ph.D thesis, Flinders University of South Australia (1989).
[17] J.P.D. Cook, I.E. McCarthy, A.T. Stelbovics and E. Weigold, J. Phys. B 17 (1984) 2339.
[18] P. Duffy, D.P. Chong, M.E. Casida and D.R. Salahub, Phys. Rev. A (1994), in press, and references therein.
[19] P. Dahl and J. Avery, Local density approximations in quantum chemistry and solid state physics (Plenum Press, New York, 1984).
[20] J.K. Labanowski and J.W. Andzelm, eds., Density functional methods in chemistry (Springer, New York, 1991).
[21] G.J. Laming, V. Termath and N.C. Handy, J. Chem. Phys. 99 (1993) 8765.
[22] N. Matsuzawa and D.A. Dixon, J. Phys. Chem. 98 (1994) 2545.
[23] M.E. Casida, Phys. Rev. A (1994), submitted for publication.

[24] G. Bieri, L. Åsbrink and W. von Niessen, J. Elec. Spectry. Relat. Phenom. 27 (1982) 129.

[25] J.A. Simpson, Rev. Sci. Instr. 35 (1964) 1698.

[26] S.D. Kevan, Rev. Sci. Instr. 54 (1983) 1441.

[27] J.L. Wiza, Nucl. Instr. Methods 162 (1979) 587.

[28] C.W. Gear, Proc. Skytop Conf. on Computer System in Experimental Nuclear Physics (usaec, 1969) p. 552.

[29] I.E. McCarthy and E. Weigold, Phys. Rev. A 31 (1985) 160.

[30] S. Chakravorty and E.R. Davidson, unpublished work.

[31] P. Duffy, M.E. Casida, C.E. Brion and D.P. Chong, Chem. Phys. 159 (1992) 347.

[32] T. Iijima and M. Kimura, Bull. Chem. Soc. Japan 42 (1968) 2159.

[33] T. Iijima, Bull. Chem. Soc. Japan 45 (1972) 3526.

[34] W.J. Hehre, R.F. Stewart and J.A. Pople, J. Chem. Phys. 51 (1969) 2657.

[35] R. Ditchfield, W.J. Hehre and J.A. Pople, J. Chem. Phys. 54 (1971) 724.

[36] R. Krishnan, M.J. Frisch and J.A. Pople, J. Chem. Phys. 72 (1980) 4244.

[37] H. Partridge, Near-Hartree–Fock quality GTO basis sets for the first- and second-row atoms, NASA Technical Memorandum 101044 (1989).

[38] J. Almlof and P.R. Taylor, J. Chem. Phys. 87 (1987) 4070.

[39] P. Duffy and D.P. Chong, Org. Mass Spectry. 28 (1994) 321.

[40] D. Feller, C.M. Boyle and E.R. Davidson, J. Chem. Phys. 86 (1987) 3424.

[41] K. Kimura, S. Katsumata, Y. Achiba, T. Yamazaki and S. Iwata, Handbook of HeI photoelectron spectra of fundamental organic molecules (Halsted Press, New York, 1981).

[42] K. Fukui, Accounts Chem. 4 (1971) 57.

[43] R.B. Woodward and R. Hoffmann, The conservation of orbital symmetry (Verlag Chemie, Weinheim, 1970).

[44] M.E. Casida and D.P. Chong, Chem. Phys. 132 (1989) 391.

[45] C.L. French, C.E. Brion and E.R. Davidson, Chem. Phys. 122 (1988) 247.

[46] Y. Zheng, F. Weigold and W. von Niessen, Chem. Phys. 184 (1994) 13.

[47] Y. Zheng, J.J. Neville and C.E. Brion, to be published.

[48] J.D. Swalen and C.C. Costain, J. Chem. Phys. 31 (1959) 1562.

[49] P. Holhenberg and W. Kohn, Phys. Rev. 136 (1964) B864.